

Survey of Gravitationally lensed Objects in HSC Imaging (SuGOHI)

IV. Lensed quasar search in the HSC survey

James H. H. Chan^{1,2,3}, Sherry H. Suyu^{4,5,3}, Alessandro Sonnenfeld^{6,7}, Anton T. Jaelani^{8,9,10}, Anupreet More^{7,11}, Atsunori Yonehara¹², Yuriko Kubota¹², Jean Coupon¹³, Chien-Hsiu Lee¹⁴, Masamune Oguri^{7,15,16}, Cristian E. Rusu¹⁷, and Kenneth C. Wong^{7,17}

¹ Institute of Physics, Laboratory of Astrophysique, École Polytechnique Fédérale de Lausanne (EPFL), Observatoire de Sauverny, 1290 Versoix, Switzerland
e-mail: hung-hsu.chan@epfl.ch

² Department of Physics, National Taiwan University, 10617 Taipei, Taiwan

³ Academia Sinica Institute of Astronomy and Astrophysics (ASIAA), 11F of ASMA, No. 1, Section 4, Roosevelt Road, Taipei 10617, Taiwan

⁴ Max-Planck-Institut für Astrophysik, Karl-Schwarzschild-Str. 1, 85748 Garching, Germany

⁵ Physik-Department, Technische Universität München, James-Frank-Str. 1, 85748 Garching, Germany

⁶ Leiden Observatory, Leiden University, Niels Bohrweg 2, 2333 CA Leiden, The Netherlands

⁷ Kavli IPMU (WPI), UTIAS, The University of Tokyo, Kashiwa, Chiba 277-8583, Japan

⁸ Department of Physics, Kindai University, 3-4-1 Kowakae, Higashi-Osaka, Osaka 577-8502, Japan

⁹ Astronomical Institute, Tohoku University, Aramaki, Aoba, Sendai 980-8578, Japan

¹⁰ Astronomy Study Program and Bosscha Observatory, FMIPA, Institut Teknologi Bandung, Jl. Ganesha 10, Bandung 40132, Indonesia

¹¹ The Inter-University Center for Astronomy and Astrophysics, Post Bag 4, Ganeshkhind, Pune 411007, India

¹² Department of Physics, Faculty of Science, Kyoto Sangyo University, 603-8555 Kyoto, Japan

¹³ Department of Astronomy, University of Geneva, ch. d'Écogia 16, 1290 Versoix, Switzerland

¹⁴ NSF's National Optical-Infrared Astronomy Laboratory, 950 N Cherry Ave, Tucson, AZ 85719, USA

¹⁵ Department of Physics, University of Tokyo, 7-3-1 Hongo, Bunkyo-ku, Tokyo 113-0033, Japan

¹⁶ Research Center for the Early Universe, University of Tokyo, 7-3-1 Hongo, Bunkyo-ku, Tokyo 113-0033, Japan

¹⁷ National Astronomical Observatory of Japan, 2-21-1 Osawa, Mitaka, Tokyo 181-8588, Japan

Received 31 October 2019 / Accepted 31 January 2020

ABSTRACT

Strong gravitationally lensed quasars provide a powerful means to study galaxy evolution and cosmology. We use CHITAH, which is an algorithm used to hunt for new lens systems, particularly lensed quasars, in the Hyper Suprime-Cam Subaru Strategic Program (HSC SSP) S16A. We present 46 lens candidates, of which 3 are previously known. We select four high-grade candidates from CHITAH for spectroscopic follow-up observations, and include two additional lenses found by YATTALENS, an algorithm used to classify lensed galaxies. We obtain X-shooter spectra of these six promising candidates for lens confirmation and redshift measurements. We report new spectroscopic redshift measurements for both the lens and source galaxies in four lens systems. We apply the lens modeling software GLEE to model our six X-shooter lenses uniformly. Through our analysis of the HSC images, we find that HSCJ022622–042522, HSCJ115252+004733, and HSCJ141136–010216 have point-like lensed images, and that the lens light distribution is well aligned with the lens mass distribution within 6 deg. We estimate the fluxes of the lensed source emission lines using X-shooter spectra, and use line ratio as a diagnostic on the Baldwin-Phillips-Terlevich (BPT) diagram. As a result, we find that HSCJ022622–042522 has a probable quasar source based on the upper limit of the [NII] flux intensity. We also measure the FWHM of Ly α emission of HSCJ141136–010216 to be ~ 233 km s⁻¹, showing that it is a probable Lyman- α emitter.

Key words. gravitational lensing; strong

1. Introduction

Strong gravitationally lensed quasars, though very rare, provide a powerful means to study both galaxy evolution and cosmology. For galaxy evolution, we can study galaxy mass structures and substructures through the use of the positions, shapes, and fluxes of lensed images (e.g., Suyu et al. 2012; Dalal & Kochanek 2002; Vegetti et al. 2012; Nierenberg et al. 2017; Gilman et al. 2019). For cosmology, measuring time delays between multiple images allows us to determine the time-delay distance and

infer the Hubble constant, H_0 (e.g., Refsdal 1964; Courbin et al. 2011; Suyu et al. 2010, 2013; Bonvin et al. 2017; Chen et al. 2019; Wong et al. 2019). The Hubble constant is a crucial cosmological parameter that sets the age, size, and critical density of the Universe, and measuring it independently through lensed quasars is important given the current tensions in its measurement (e.g., Planck Collaboration VI 2020; Riess et al. 2019; Freedman et al. 2019; Wong et al. 2019). Further, quasar microlensing events which are expected to arise frequently in lensed quasars enable us to investigate various

astrophysical questions, such as those pertaining to the structure of the quasar central engine (e.g., Yonehara et al. 1998; Mineshige & Yonehara 1999; Poindexter et al. 2008), the mass function of stars in galaxies (e.g., Wyithe et al. 2000), and extra-galactic planet detection (e.g., Dai & Guerras 2018).

There have been several undertakings to look for such events in various surveys. The Cosmic Lens All-sky Survey (CLASS; Myers et al. 2003) discovered the largest statistical sample of radio-loud gravitational lenses by obtaining high-resolution images of flat-spectrum radio sources and identifying the ones that showed multiple images. In the optical, the SDSS Quasar Lens Search (SQLS; e.g., Oguri et al. 2006, 2008, 2012; Inada et al. 2008, 2010, 2012) obtained the largest lensed quasar sample to date based on both morphological and color selection of spectroscopically confirmed quasars. Jackson et al. (2012) further combined the quasar samples from the SDSS and the UKIRT Infrared Deep Sky Survey (UKIDSS) to find small-separation or high-flux-ratio lenses. Data mining on catalog magnitudes also provides an opportunity to find lensed quasars (Agnello et al. 2015; Agnello 2017; Ostrovski et al. 2017; Williams et al. 2018). Chan et al. (2015) built CHITAH to inspect image configurations using lens modeling, which was first demonstrated by Marshall et al. (2009) who detected lenses in the *Hubble* Space Telescope (HST) archival images.

Another systematic approach has been proposed by Kochanek et al. (2006) where all extended variable sources are identified as potential lenses. Chao et al. (2019) have built an algorithm using the extent of variable sources in the difference images of the ongoing Hyper-Suprime Cam (HSC) Transient Survey. In addition, the recent data releases of *Gaia*, with its exceptional resolution, provide an efficient way to find lensed quasars (e.g., Ducourant et al. 2018a,b; Krone-Martins et al. 2018). One could conduct a quasar lens search by looking for multiple detection in *Gaia* or comparing the flux and position offsets from other surveys (e.g., Lemon et al. 2017, 2018, 2019; Delchambre et al. 2019). Although not specific to lensed quasars, SPACE WARPS (Marshall et al. 2016; More et al. 2016) show that lensed quasars could also be found through citizen science.

We present a new lens sample as part of the Survey of Gravitationally lensed Objects in HSC Imaging (SuGOHI) that aims to find lenses at both galaxy- and cluster-mass scales. Most of the candidates in this paper are classified by CHITAH, and we refer to this corresponding sample of lenses as the SuGOHI lensed quasar sample, or SuGOHI-q. The first SuGOHI galaxy-scale sample (SuGOHI-g) is presented in Sonnenfeld et al. (2018), with subsequently discovered lenses described in Wong et al. (2018). In an upcoming paper, we will present a new sample of lenses obtained by looking at clusters of galaxies (SuGOHI-c, Jaelani et al., in prep.).

This paper is organized as follows. In Sect. 2, we briefly introduce the HSC survey. The preselection methods are described in Sect. 3. We summarise the machinery of the CHITAH algorithm and present the candidate lens systems in Sect. 4. The X-shooter follow-up is described in Sect. 5. We confirm our lens systems in Sect. 6. We conclude in Sect. 7. All images are oriented with north up and east to the left. Magnitudes quoted in this paper are in AB magnitudes.

2. The Hyper-Suprime Cam survey

The HSC has 104 science CCDs covering a field of view of 1.5 deg in diameter with a 0.168'' pixel scale for the 8.2 m Subaru telescope (Miyazaki et al. 2018; Komiyama et al. 2018;

Kawanomoto et al. 2018; Furusawa et al. 2018). The Hyper Suprime-Cam Subaru Strategic Program (HSC-SSP) Survey consists of three layers (Wide, Deep, and Ultradeep), and the Wide layer is planned to observe a sky area of $\sim 1400 \text{ deg}^2$ in five broadband filters (*grizy*) (see details in Aihara et al. 2018). We use imaging data from the S16A data release covering 456 deg^2 from all five bands, 178 deg^2 of which has full color to the target depth $r \approx 26$. The median seeing in the *i*-band is about 0.6''. The data are reduced using the pipeline hscPipe (Bosch et al. 2018). Although data from the S16A release are not publicly available at the time of working on this project, most of the lens candidates presented in this work are visible in the public data release 1 (PDR1).

3. Preselection method

Before running CHITAH, we pre-select our targets to speed up the classification. The beginning sample comes from either the catalogs with possible lens galaxies, or the catalogs with possible quasar sources. For the possible lens galaxies, we select the luminous red galaxies (LRG) from the SDSS BOSS spectrograph. For the possible quasar sources, we use the SDSS+WISE photometry.

3.1. Luminous red galaxies in BOSS spectroscopy

One of the reasons that we chose LRGs is that LRGs are massive galaxies that have a large strong lensing cross section ($\propto \sigma^4$, where σ is the velocity dispersion). Also, LRGs are bright and highly visible at higher redshifts. Therefore, there is a bias toward the most massive galaxies.

The BOSS survey provides two principle galaxy samples: the low-redshift (LOWZ) and high-redshift (CMASS) samples, respectively (Reid et al. 2016). The main difference between the two samples is mostly the redshift distribution: LOWZ galaxies are mostly at $z < 0.4$ while CMASS galaxies are mostly in the range $0.4 < z < 0.7$. The number of BOSS galaxies with photometry in all five bands of the 2016A data release of HSC is about 43 000, of which approximately 9000 are from LOWZ and approximately 34 000 are from CMASS. We include one more LRG catalog provided by Kazin et al. (2010)¹, which has approximately 2000 objects.

3.2. Quasars with the SDSS+WISE photometry

To find lensed quasar systems that do not have lens galaxies identified as LRGs, we further perform photometric selection of quasar candidates from SDSS Data Release 14 (Abolfathi et al. 2018) using a nonparametric Bayesian classification method (e.g., Richards et al. 2004) which incorporates a kernel density estimate (KDE; Silverman 1986).

Photometric data from SDSS are taken under substantially poorer seeing conditions compared to HSC survey data, and images of lensed quasar systems in SDSS data are expected to show extended structures due to foreground lens galaxies and/or multiple images of the lensed quasar. Therefore, in our photometric selection of quasar candidates, we do not take into account any morphological information such as the probability that the object is point-like (which is often used in the selection of unlensed quasars). Another reason we use SDSS photometry is that it provides *u*-band data which allow us to select a cleaner sample of quasars. Through only photometric data, we classify

¹ <https://cosmo.nyu.edu/~eak306/SDSS-LRG.html>

objects in the photometric catalog into three categories: star (S), galaxy (G), and quasar (Q). For objects with photometric data \mathbf{x} , the probability of an object being in category $i = S, G,$ or Q is evaluated using

$$P(i|\mathbf{x}) = \frac{P(\mathbf{x}|i)P(i)}{\sum_i P(\mathbf{x}|i)P(i)}, \quad (1)$$

where $P(\mathbf{x}|i)$ and $P(i)$ are the probability density function (PDF) for category i and the probability that the object is in category i , respectively. To obtain the PDF for any given photometric data \mathbf{x} , we apply KDE with the following form:

$$P(\mathbf{x}|i) = \frac{1}{N_i} \sum_{k=1}^{N_i} \frac{1}{\sqrt{2\pi}h} \exp\left(-\frac{|\mathbf{x} - \mathbf{x}_k|}{2h^2}\right), \quad (2)$$

where N_i is the number of objects in category i , \mathbf{x}_k is the photometric data of the k th object in the category, and h is a scaling factor of the kernel function. In the current study, five independent colors, $u - g$, $g - r$, $r - i$, and $i - z$ in SDSS photometry, and W1–W2 in WISE photometry, are used for photometric data \mathbf{x} , and h is set to 0.1 to maximize the classification accuracy.

Here, we use the SDSS-DR14 spectroscopic catalog with WISE photometry, which includes spectroscopically confirmed objects (138 055 quasars, 939 101 galaxies, and 187 431 stars). Our final target is multiple quasars behind lens galaxies, and images of such objects are expected to show extended source-like morphology. Therefore, we selected the cModelMag magnitude from the SDSS catalog as the magnitude of objects, and have not put any constraint on the source extent such as probPSF in the SDSS catalog. Half of spectroscopically confirmed objects are used as a training data set to construct the PDF, and the remaining half are used as a test data set to evaluate proper threshold for $P(Q|\mathbf{x})$ to select as many quasar candidates as possible with high classification accuracy. It is not easy to estimate the true value of $P(i)$ in the real Universe because of several biases, and we set $P(i)$ based on the spectroscopic sample we used. While this is simple, our result does not dramatically change in cases where we assume a real number of galaxies that is ten times larger than the galaxies in the spectroscopic sample. After several estimations using the data sets, we set $P(Q|\mathbf{x}) \geq 0.9$ as a threshold for quasar candidate selection. With this threshold value, we are expected to obtain a set of quasar candidates that includes $\sim 75\%$ of all quasars, with $\sim 95\%$ purity (fraction of quasars in all objects classified as ‘‘quasar’’). We evaluate $P(i|\mathbf{x})$ for all objects in the SDSS-DR14 photometric catalog with WISE photometry, and obtain quasar candidates of $P(Q|\mathbf{x}) \geq 0.9$. As this selection method can also find $\geq 80\%$ of already known lensed quasars in the SDSS photometric objects with WISE photometry, the light from lens galaxies must not seriously degrade the selection performance. In the HSC S16A region, the number of quasar candidates is approximately 76 000 in a total of about 3 000 000 objects.

We include one more QSO catalog with about 34 000 QSOs provided by [Brescia et al. \(2015\)](#)² using the Multi Layer Perceptron with Quasi Newton Algorithm (MLPQNA) method and the optical data of SDSS DR10.

4. CHITAH performance: promising candidates after visual inspection

CHITAH ([Chan et al. 2015](#)) is a lens hunter in imaging surveys, that is, it searches for lensed quasar systems based on the configuration of lensed images. We briefly describe the procedure of

CHITAH in Sect. 4.1, and the grading system in Sect. 4.2. A few additional candidates found through other means are described in Sect. 4.3. In this work, we focus on quad (four-image) systems using CHITAH.

4.1. CHITAH: strong-gravitational-lens hunter

The procedure of CHITAH is as follows:

First it chooses two image cutouts, one from bluer bands (g/r) and one from redder bands (z/y) based on which band has a sharper point-spread function (PSF). All cutouts are from HSC. CHITAH then matches PSFs in the two selected bands, and disentangles lens light and lensed images according to color information. CHITAH then identifies lens center and lensed image positions, masking out the region within $0.5''$ in radius from the lens center in the lensed arc image to prevent misidentifying lensed image positions near the lens center because of imperfect lens light separation. Finally, CHITAH models the lensed-image configuration with a singular isothermal elliptical (SIE) lens mass distribution. The outputs of the model are the best-fit parameters of the SIE: the Einstein radius (θ_{Ein}), the axis ratio (q), the position angle (PA), and the lens center. The two-dimensional surface mass density of the SIE is expressed as:

$$\kappa = \frac{\theta_{\text{Ein}}}{2\sqrt{\theta_1^2 + \theta_2^2/q^2}}, \quad (3)$$

where (θ_1, θ_2) are the coordinates relative to the lens center along the semi-major and semi-minor axes of the elliptical mass distribution. We determine the SIE model parameters by minimizing the χ^2_{src} on the source plane, which is defined as

$$\chi^2_{\text{src}} = \sum_k \frac{|\beta_k - \beta_{\text{model}}|^2}{\sigma_{\text{image}}^2/\mu_k}, \quad (4)$$

where β_k is the respective source position mapped from the position of lensed image k , μ_k is the magnification at the position of lensed image k , σ_{image} is chosen to be the pixel scale of HSC ($0.168''$) as an estimate of the uncertainty, and β_{model} is the modeled source position evaluated as a weighted mean of β_k ,

$$\beta_{\text{model}} = \frac{\sum_k \sqrt{\mu_k} \beta_k}{\sum_k \sqrt{\mu_k}}, \quad (5)$$

([Oguri 2010](#)). Here the value of the index k runs from 1 to 4 for quad systems. We also use the lens center from the light profile as a prior to constrain the center of the SIE lens mass model. Therefore, we define the χ^2_{c} as

$$\chi^2_{\text{c}} = \frac{|\mathbf{x}_{\text{model}} - \mathbf{x}_{\text{c}}|^2}{\sigma_{\text{c}}^2}, \quad (6)$$

where \mathbf{x}_{c} is the lens center from the light profile, and $\mathbf{x}_{\text{model}}$ is the lens center of the SIE model. We choose σ_{c} to be the same as σ_{image} . We further take into account the residuals of the fit to the ‘‘lensed arc’’ image from CHITAH. The difference between the lensed image intensity $I(i, j)$ and the predicted image intensity $I^{\text{P}}(i, j)$ is defined as,

$$\chi^2_{\text{res}} = \sum_{i,j} \frac{[I(i, j) - I^{\text{P}}(i, j)]^2}{\text{var}(i, j)}, \quad (7)$$

where $i = 1 \dots N_x$ and $j = 1 \dots N_y$ are the pixel indices in the image cutout of dimensions $N_x \times N_y$, and $\text{var}(i, j)$ is the pixel

² http://dame.fisica.unina.it/dame_qso.html

uncertainty in $I(i, j)$. We note that I is obtained from possible lensed images according to color information, and I^P is obtained from PSF fitting instead of the lens modeling; see Fig. 1d in Chan et al. (2015). Therefore, the fluxes of the lensed image are not affected by flux anomalies.

The criteria of classification of lens candidates are $\chi_{\text{src}}^2 + \chi_{\text{c}}^2 < 2\theta_{\text{Ein}}$, where θ_{Ein} is measured in arcsec, and $\chi_{\text{res}}^2 < 100$. The former criterion allows CHITAH to detect lens candidates covering a wide range of θ_{Ein} , since typically χ_{src}^2 scales with θ_{Ein} and our tests with mock systems in Chan et al. (2015) show that $\chi_{\text{src}}^2 \lesssim 4$ yields a low false-positive rate of $< 3\%$. The latter criterion allows us to further eliminate false positives. The lens candidates are selected within $0.3'' < \theta_{\text{Ein}} < 4''$.

4.2. Grading candidates identified by CHITAH

We begin with the preselection catalogs, and then we extract stamps ($7'' \times 7''$) from HSC imaging, including the science images in g, r, i, z , and y -bands, the variance images, and the corresponding PSFs. We begin from the LRG catalogs with approximately 45 000 objects and from the QSO catalogs with approximately 110 000 objects. After CHITAH's classification, we obtain 800 candidates from LRG catalogs and 3400 candidates from QSO catalogs. The classification rate is 1.5% and 3.1%, respectively. First, J. H. H. C. remove those candidates that are clearly not lenses but are classified as lenses by CHITAH because of imperfect PSF matching and nearby objects in cutouts. This false detection can be improved by pre-selection methods. After that, we grade candidates from "0" to "3", according to the following rule:

- 3: almost certainly a lens,
- 2: probably a lens,
- 1: possibly a lens,
- 0: non-lens.

Typical aspects taken into consideration in grading are the residual from lens removal and the positions of possible lensed images. Nine coauthors independently graded each candidate, assigning a score of between 0 and 3 at increments of 0.5, similarly to Sonnenfeld et al. (2018). We list our 46 candidates with grades ≥ 1.5 in Table 1, and show them in Fig. 1. Most of our candidates from LRG catalogs are also found by YATTALENS and were presented in Sonnenfeld et al. (2018). We notice that the LRG pre-selection tends to provide spatially extended lensed sources. In the QSO pre-selection, there are some clear point sources. The scaled Einstein radii (θ_{Ein}^s) are listed in Col. 4 of Table 1:

$$\theta_{\text{Ein}}^s = \theta_{\text{Ein}} \sqrt{\frac{2q^2}{1+q^2}}. \quad (8)$$

4.3. Other candidates

There are three known lenses in the HSC S16A footprint found again by CHITAH: HSCJ092455+021923 (Inada et al. 2012), HSCJ095921+020638 (Anguita et al. 2009), and HSCJ115252+004733 (More et al. 2017)³. We include two new lens candidates, HSCJ091148+041852 and HSCJ141136–010216, found by YATTALENS but missed in CHITAH's classification⁴ for

³ We observed HSCJ115252+004733 again to determine the nature of its source.

⁴ HSCJ091148+041852 is preselected from SPACE WARPS in the HSC survey (Sonnenfeld et al., in prep.). CHITAH missed HSCJ141136–010216 since the lensed images are too faint.

X-shooter spectroscopic follow-up. We present these candidates in Fig. 1c.

5. X-shooter spectroscopic follow-up

To decipher the nature of the lensed candidates, we used the ESO VLT facility with the X-shooter spectrograph (Vernet et al. 2011). The main goal of this programme (ESO programme 099.A-0220, PI: Suyu) is to measure the redshifts of lens galaxies and lensed background sources (Sonnenfeld et al. 2019). From the list of lens candidates described in the previous section, we picked out the candidates that have probable point-like sources. In total, we observed six lens candidates, including four high-grade candidates from CHITAH and two additional lenses by YATTALENS. These are the top-ranked lensed quasar candidates that we were able to observe within the available observing time.

We observed each target in slit mode with two observation blocks (OBs), except for HSCJ115252+004733 which could only be observed in one OB due to bad weather. Each OB corresponds to roughly one hour of telescope time, and consists of 10×285 s exposures obtained in an ABBA nodding pattern to optimise background subtraction in the near-infrared (NIR) arm. Exposure times in the UVB and VIS arms are slightly shorter due to the longer readout time. We used slit widths of $1.0''$, $0.9''$, and $0.9''$ in the UVB, VIS, and NIR arms respectively, and applied a 2×2 pixel binning to the UVB and VIS CCDs. We positioned the slit so that it covered both the center of the lens galaxy and the brightest feature of the lensed source. Observations were executed with a seeing of $FWHM < 0.9''$ on target position.

We reduced the 2D spectra to 1D by processing the raw data using ESO ReflEx software version 2.9.0 combined with the X-shooter pipeline recipes version 3.1.0 (Freudling et al. 2013). In general, the pipeline recipes perform standard bias subtraction, flat-fielding of the raw spectra, and wavelength calibration. Cosmic rays were removed using LACosmic (van Dokkum 2001). We calibrated the flux based on a spectroscopic standard star. For further data processing and analysis, we used standard IRAF tools. We stacked each 2D single-exposure spectrum of two OBs, and produced 1D spectra using an extraction aperture in all three arms. The flux errors were calculated using error propagation from the raw image until extracting the 1D spectra.

The 1D spectra of the lens galaxies and lensed sources of the six candidates are shown in Figs. 2 and 3. The extraction apertures for 1D spectra are shown by the red, blue, and green areas in the 2D spectrum for the lensed source, its counterpart, and the lens galaxy, respectively, in Fig. 3.

6. New lens systems

After inspecting the spectra of the six candidates, we confirm that five of them have the same spectra for the lensed source and its counterpart, except for HSCJ144320–012538. However, this latter object has a clear lensing feature as shown in Fig. 1, even though we do not obtain the spectrum of its counter image because it is too faint.

The X-shooter spectra allow us to measure the redshifts of both the lens and source galaxies. To do so, we smooth the stacked 2D spectrum that have spectral resolutions of 0.6 \AA pix^{-1} in NIR and 0.2 \AA pix^{-1} in UVB and VIS using a box kernel of 4 \AA width, and fit Gaussian profiles on G, H, and K lines for the lens galaxies and detectable emission lines for the lensed sources. We list

Table 1. Lens candidates from CHITAH.

| Name | RA [deg] | Dec [deg] | θ_{Ein}^s | Grade | Preselection | Comment |
|--------------------------------|----------|-----------|-------------------------|-------|----------------------------|--------------------------|
| HSCJ095921+020638 | 149.841 | 2.111 | 0.69'' | 3.0 | – | Anguita et al. (2009) |
| HSCJ115252+004733 [†] | 178.218 | 0.793 | 1.39'' | 3.0 | – | More et al. (2017) |
| HSCJ090507–001030 | 136.281 | –0.175 | 1.23'' | 2.1 | LRG: CMASS | Sonnenfeld et al. (2018) |
| HSCJ090709+005648 | 136.790 | 0.947 | 1.32'' | 2.4 | LRG: CMASS | Sonnenfeld et al. (2018) |
| HSCJ144307–004056 | 220.780 | –0.682 | 1.03'' | 2.1 | LRG: CMASS | Sonnenfeld et al. (2018) |
| HSCJ143153–013353 | 217.973 | –1.565 | 2.78'' | 1.8 | LRG: CMASS | Sonnenfeld et al. (2018) |
| HSCJ083943+004740 | 129.929 | 0.795 | 1.40'' | 1.7 | LRG: CMASS | Sonnenfeld et al. (2018) |
| HSCJ223406+012057 | 338.529 | 1.349 | 1.24'' | 1.6 | LRG: CMASS | Sonnenfeld et al. (2018) |
| HSCJ222801+012805 | 337.008 | 1.468 | 1.60'' | 2.6 | LRG: CMASS | Sonnenfeld et al. (2018) |
| HSCJ023817–054555 [†] | 39.574 | –5.765 | 0.92'' | 2.8 | LRG: CMASS | Sonnenfeld et al. (2018) |
| HSCJ023307–043838 | 38.279 | –4.644 | 1.65'' | 1.8 | LRG: CMASS | – |
| HSCJ021200–040806 | 33.004 | –4.135 | 1.59'' | 1.5 | LRG: CMASS | Sonnenfeld et al. (2018) |
| HSCJ144230–002353 | 220.629 | –0.398 | 1.17'' | 1.6 | LRG: LOWZ | – |
| HSCJ224221+001144 | 340.590 | 0.196 | 1.41'' | 2.9 | LRG: LOWZ | Sonnenfeld et al. (2018) |
| HSCJ223359+015826 | 338.500 | 1.974 | 0.85'' | 1.5 | LRG: LOWZ | Sonnenfeld et al. (2018) |
| HSCJ015756–021809 | 29.486 | –2.303 | 1.07'' | 1.8 | LRG: LOWZ | Sonnenfeld et al. (2018) |
| HSCJ022511–045433 | 36.296 | –4.909 | 1.53'' | 2.1 | LRG: LOWZ | – |
| HSCJ163257+424611 | 248.241 | 42.770 | 1.64'' | 3.0 | LRG: Kazin et al. (2010) | – |
| HSCJ090613+032939 | 136.555 | 3.494 | 0.94'' | 1.6 | LRG: CMASS | Sonnenfeld et al. (2018) |
| HSCJ091506+041716 | 138.776 | 4.288 | 1.23'' | 1.5 | LRG: CMASS | Sonnenfeld et al. (2018) |
| HSCJ091608+034710 | 139.036 | 3.786 | 1.15'' | 2.9 | LRG: CMASS | Sonnenfeld et al. (2018) |
| HSCJ092101+035521 | 140.256 | 3.923 | 1.21'' | 2.6 | LRG: CMASS | Sonnenfeld et al. (2018) |
| HSCJ121052–011904 | 182.718 | –1.318 | 1.16'' | 2.6 | LRG: CMASS | – |
| HSCJ140929–011410 | 212.374 | –1.236 | 1.24'' | 3.0 | LRG: CMASS | Sonnenfeld et al. (2018) |
| HSCJ141300–012608 | 213.250 | –1.436 | 1.13'' | 2.8 | LRG: CMASS | Sonnenfeld et al. (2018) |
| HSCJ145732–015917 | 224.386 | –1.988 | 1.20'' | 3.0 | LRG: CMASS | Sonnenfeld et al. (2018) |
| HSCJ155517+415138 | 238.824 | 41.861 | 1.31'' | 3.0 | LRG: CMASS | Sonnenfeld et al. (2018) |
| HSCJ155826+432830 | 239.611 | 43.475 | 1.41'' | 2.0 | LRG: CMASS | Sonnenfeld et al. (2018) |
| HSCJ092455+021923 | 141.233 | 2.323 | 0.84'' | 3.0 | – | Inada et al. (2003) |
| HSCJ022059–045554 | 35.249 | –4.932 | 1.02'' | 1.6 | QSO: SDSS+WISE | – |
| HSCJ022622–042522 [†] | 36.593 | –4.423 | 0.81'' | 2.6 | QSO: SDSS+WISE | – |
| HSCJ221608+005538 | 334.036 | 0.927 | 0.65'' | 2.6 | QSO: SDSS+WISE | – |
| HSCJ222022+000710 | 335.095 | 0.120 | 0.62'' | 1.7 | QSO: SDSS+WISE | – |
| HSCJ222618–011940 | 336.576 | –1.328 | 0.57'' | 1.6 | QSO: SDSS+WISE | – |
| HSCJ162757+435849 | 246.988 | 43.980 | 0.52'' | 1.8 | QSO: SDSS+WISE | – |
| HSCJ161955+431024 | 244.982 | 43.173 | 0.77'' | 1.7 | QSO: SDSS+WISE | – |
| HSCJ022040–052056 | 35.168 | –5.349 | 0.96'' | 1.7 | QSO: SDSS+WISE | – |
| HSCJ090412+000420 | 136.051 | 0.072 | 0.55'' | 1.6 | QSO: SDSS+WISE | – |
| HSCJ115943+012846 | 179.931 | 1.479 | 0.57'' | 1.8 | QSO: SDSS+WISE | – |
| HSCJ120045–005740 | 180.189 | –0.961 | 1.57'' | 1.9 | QSO: SDSS+WISE | – |
| HSCJ115312+000206 | 178.304 | 0.035 | 0.58'' | 1.6 | QSO: SDSS+WISE | – |
| HSCJ115530+004141 | 178.879 | 0.695 | 0.64'' | 1.6 | QSO: Brescia et al. (2015) | – |
| HSCJ221606+023139 | 334.026 | 2.528 | 0.58'' | 1.8 | QSO: Brescia et al. (2015) | – |
| HSCJ083906–000000 | 129.777 | –0.000 | 1.84'' | 1.8 | QSO: SDSS+WISE | – |
| HSCJ090710+000320 | 136.794 | 0.056 | 0.66'' | 1.8 | QSO: SDSS+WISE | – |
| HSCJ144320–012538 [†] | 220.836 | –1.427 | 1.02'' | 2.7 | QSO: SDSS+WISE | – |
| HSCJ091148+041852 [†] | 137.954 | 4.315 | – | – | – | Found by YATTALENS |
| HSCJ141136–010216 [†] | 212.902 | –1.038 | – | – | – | Found by YATTALENS |

Notes. Column 4 lists θ_{Ein}^s modeled by CHITAH. Column 5 shows the average grades of nine coauthors. We include the last two candidates found by YATTALENS. We highlight candidates for which there are X-shooter spectra with †.

the measurement in Table 2. Evidently, the bluer lensed features are at higher redshifts compared to the main galaxies. We note that our redshift measurements of HSCJ115252+004733 and HSCJ023817–054555 are consistent with those in More et al. (2017) and Sonnenfeld et al. (2019), respectively.

6.1. Lens modeling

To investigate the lensing nature of the six X-shooter lenses, we use the lens modeling software GLEE (Suyu & Halkola 2010; Suyu et al. 2012) to fit the lens light and lensed-source

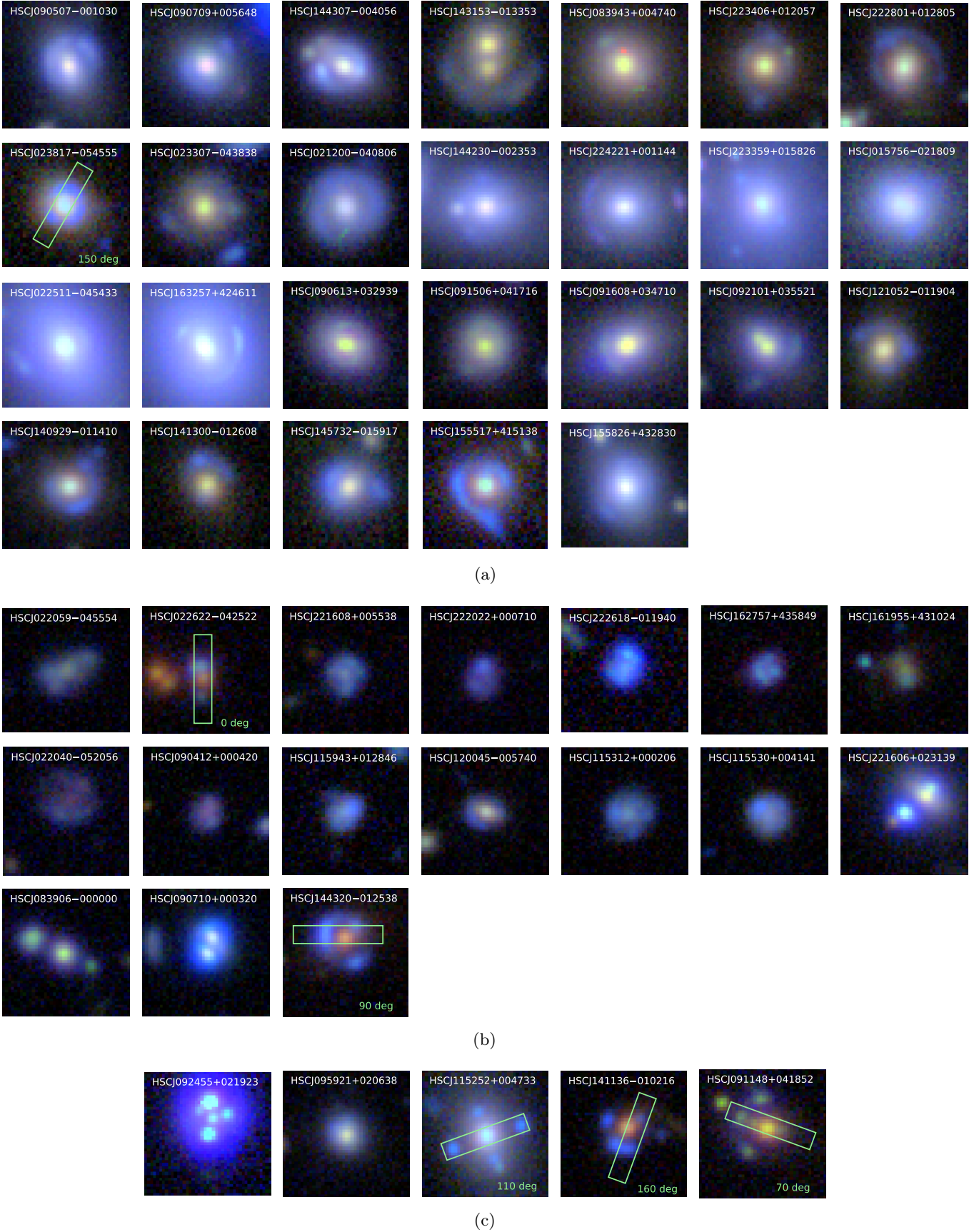


Fig. 1. Lens candidates classified by CHITAH from preselected LRGs (a) and QSOs (b). We list in (c) other candidates whose origins are noted in Table 1. Each $r_i z_j$ image cutout is $7'' \times 7''$. The green box indicates the position of the slit used during the X-shooter spectroscopic observation.

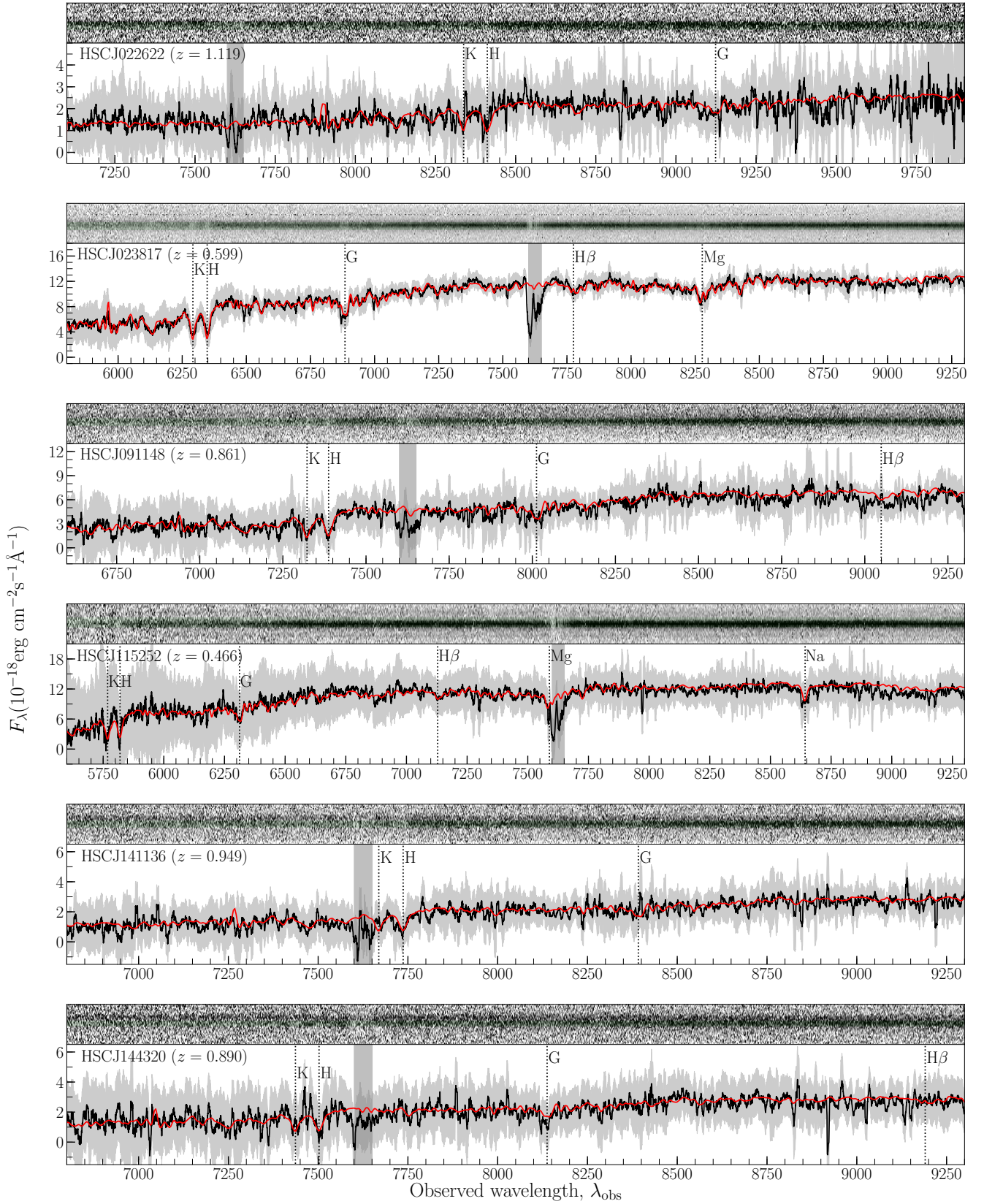


Fig. 2. Stacked 1D spectra of the X-shooter lens galaxies (black lines) with commonly found absorption features indicated (vertical dashed lines). The error on the spectrum is shown with a shaded region (gray). *Upper panel* in each row: small cutouts of the 2D spectrum with a green shaded region corresponding to the aperture for 1D spectra extraction of the lens galaxy. The vertical rectangular shaded region (gray) shown in all panels indicates absorption features probably due to telluric contamination. The lens redshift is shown in the upper-left corner of each panel. For comparison, we show a composite luminous red galaxy spectrum from [Dobos et al. \(2012\)](#) shifted by the measured redshifts, in red. The unit of the wavelength is angstroms.

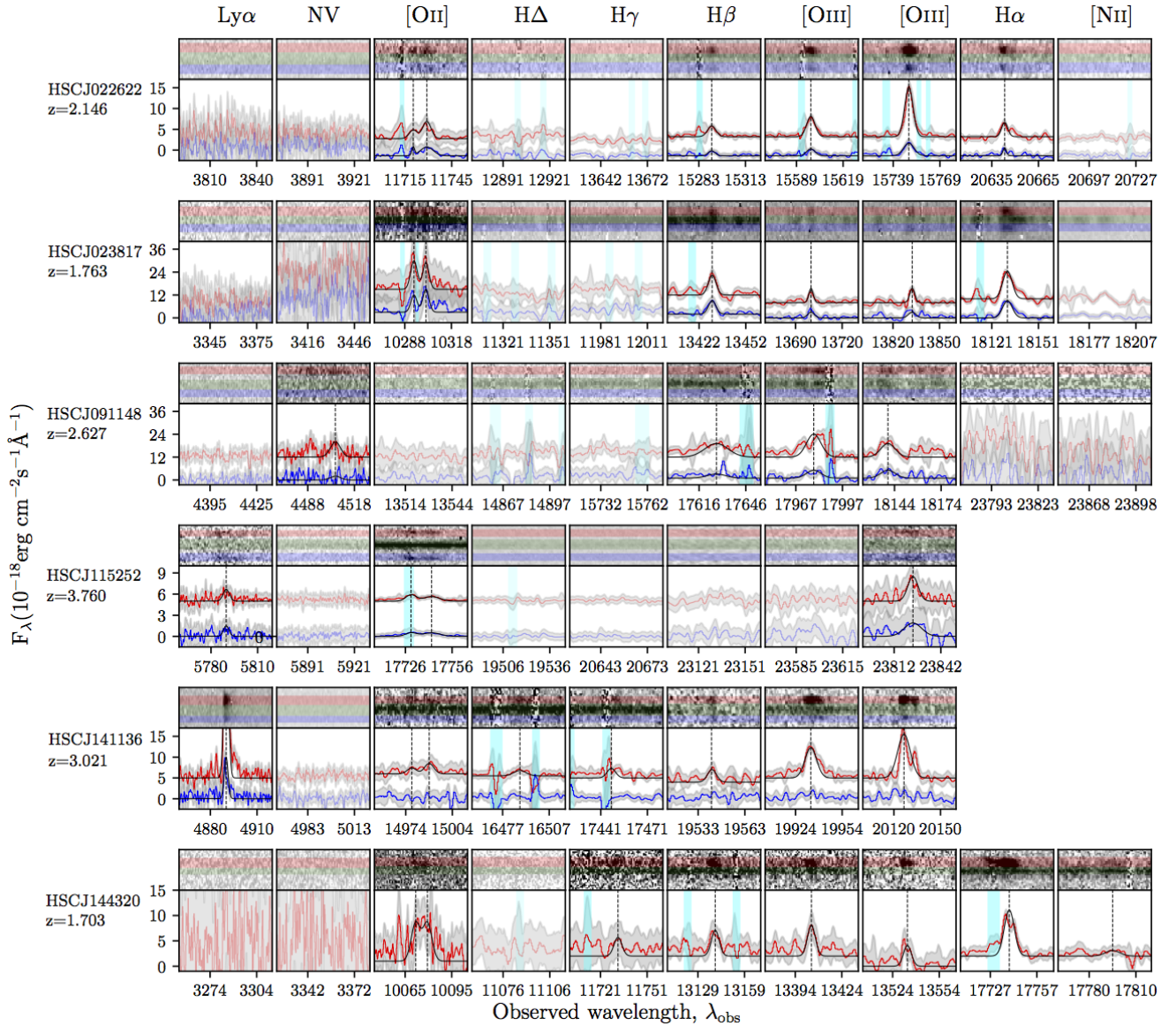


Fig. 3. *Upper panel* in each row: small cutouts of the 2D spectrum with three shaded regions (red, green, blue) which correspond to the apertures for 1D spectra extraction of lensed source, lens galaxy, and lensed counterpart, respectively. The stacked 1D spectrum of the X-shooter lensed source and its counterpart are shown with red and blue lines, respectively, in the *lower panel*, with corresponding emission lines marked by the vertical dashed lines and labeled above the panels. The errors on the spectrum are shown with a shaded region (gray). The black lines show Gaussian fits to the emission lines. The vertical shaded region (cyan) shown in all panels indicates absorption features due to telluric contamination. The semi-transparent panels show the locations of common emission lines that are not detected for the given source redshift. The unit of wavelength is angstroms.

Table 2. Lens candidates with X-shooter spectra.

| Name | z_l | z_s | $n_{\text{Sérsic}}$ | q_{light} | PA_{light} [deg] | θ_{Ein} [$''$] | q | PA [deg] | θ_{Ein}^s [$''$] | Comment |
|-------------------|--------|--------|---------------------|--------------------|-------------------------------------|-----------------------------------|------|-------------|-------------------------------------|--------------------|
| HSCJ022622–042522 | 1.119* | 2.146* | 9.13 | 0.85 | 10.28 | 1.28 | 0.56 | –8.92 | 0.88 | – |
| HSCJ023817–054555 | 0.599 | 1.763 | 2.89 | 0.85 | 51.19 | 0.99 | 0.87 | 45.17 | 0.92 | – |
| HSCJ091148+041852 | 0.861* | 2.627* | 10.00 | 0.83 | –78.45 | 2.39 | 0.40 | 74.04 | 1.24 | Found by YATTALENS |
| HSCJ115252+004733 | 0.466 | 3.760 | 3.63 | 1.00 | –86.82 | 3.28 | 0.33 | 19.22 | 1.45 | More et al. (2017) |
| HSCJ141136–010216 | 0.949* | 3.021* | 6.48 | 0.56 | –52.30 | 1.28 | 0.74 | –47.67 | 1.07 | Found by YATTALENS |
| HSCJ144320–012538 | 0.890* | 1.703* | 2.76 | 0.73 | –52.94 | 1.68 | 0.52 | –56.09 | 1.09 | – |

Notes. We measure the lens and source redshifts as shown in Cols. 2 and 3. We highlight the new redshift measurements with an asterisk. The best-fit parameter values of lens modeling from GLEE are listed in Cols. 4–9, as illustrated in Fig. 4. The corresponding scaled Einstein radius as listed in Col. 10. We allow for an additional external shear component for HSCJ022622–042522 and find $\gamma_{\text{ext}} = 0.15$ and $\text{PA}_{\text{ext}} = 52.27$ deg, due to the presence of a close-by galaxy group.

components. First, we mask out nearby galaxies for each lens, and denote the pixel intensity value of pixel (i, j) by $I^{\text{glee}}(i, j)$. We model the lens light components using Sérsic profiles and the lensed-source components using four PSFs, assuming that our candidates have point-like quasar sources denoted by $I^{\text{P,glee}}$. The best-fit values of the Sérsic index ($n_{\text{Sérsic}}$), axis ratio (q_{light}), and position angle (PA_{light}) are listed in Table 2. We also include the reduced $\chi^2_{\text{res,glee}}$ of the best-fitting model in the panels of the third column, which is defined as

$$\chi^2_{\text{res,glee}} = \frac{1}{N_{\text{pix}}} \sum_{i,j} \frac{[I^{\text{glee}}(i, j) - I^{\text{P,glee}}(i, j)]^2}{\text{var}(i, j)}, \quad (9)$$

where $i = 1 \dots N_x$, $j = 1 \dots N_y$ are the pixel, and N_{pix} is the total number of pixels without masking.

After identifying the positions of four PSFs (θ_k , where $k = 1, 2, 3, 4$), we fit the SIE lens model to the four PSF positions using the goodness of fit on the image plane:

$$\chi^2_{\text{img,glee}} = \sum_k \frac{|\theta_k - \theta_{\text{model},k}|^2}{\sigma_{\text{image}}^2}, \quad (10)$$

where $\theta_{\text{model},k}$ are the predicted positions of the lensed image from the best-fitting lens model. The reason for performing the modeling described above is to see if the lensed features can be captured by four simple PSFs. The result of GLEE is shown in Fig. 4 and the scaled Einstein radii are listed in Table 2. The first column of Fig. 4 shows the image cutout of the system in the filter with the sharpest PSF. We further mask out the nearby objects. The second column shows the model with a Sérsic lens light profile and four PSFs, and the residual is shown in the third column. The fourth column shows the best SIE model. The critical and caustic curves are shown in red solid and dash curves, respectively. The predicted positions of images and sources are labeled as orange crosses and green diamonds, respectively. The measured positions of the four PSFs are labeled as white circles. We discuss each object in detail below.

HSCJ022622–042522. The lensed images can be well fitted by PSFs. The source is likely a quasar. However, we need to impose an additional external shear component to model the image configuration because of a nearby galaxy group. We also note that the top lensed images cannot be fitted by a single PSF. Therefore this target is more likely to be a quad system. The nearby galaxy group results in a substantial difference between q_{light} and q ; see Fig. 1b.

HSCJ023817–054555. There are evident arc-like residuals, showing that the source is most likely a lensed galaxy without an AGN. This lens is also found by YATTALENS (Sonnenfeld et al. 2018). When compared to the lensing parameters from Sonnenfeld et al. (2019) with $\theta_{\text{Ein}} = 0.93''$, $q = 0.92$, and $\text{PA} = 119.8$ deg, the Einstein radius and axis ratio agree well although the PA is offset mostly because the mass distribution is quite round. The axis ratios and PAs of lens light and lens mass are comparable.

HSCJ091148+041852. The residual may come from the host galaxy of the quasar or a galaxy-scale source. The mass profile is more elliptical than the light profile due to some nearby galaxies.

HSCJ115252+004733. The lensed images can be well fitted by PSFs. The mass profile is more elliptical because of the small satellite close to the bottom lensed image. We further compare our lensing parameters to the ones from More et al. (2017):

$\theta_{\text{Ein}} = 4\pi(\frac{\sigma}{c})^2 \frac{1}{\sqrt{q}} = 3.07''$ ($\sigma = 280 \text{ km s}^{-1}$, $q = 0.54$), and $\text{PA} = 19.1$ deg, which are consistent with the result from GLEE.

HSCJ141136–010216. The residual is not prominent. The source could be point-like. The lens mass distribution is rounder, but has the same orientation as the light distribution.

HSCJ144320–012538. There are evident arc-like residuals, showing that the source is most likely a lensed galaxy without an AGN. The orientations of lens light and lens mass distribution are comparable. Here, $q_{\text{light}} > q$ is caused by imperfect lens light subtraction.

We further compare $\theta_{\text{Ein}}^{\text{S}}$ from CHITAH and GLEE. CHITAH, which can rapidly model the lenses, provides good measurements that are within <8% of the results from the more detailed modeling with GLEE. We found that three of our X-shooter lenses have well aligned light and mass distribution (<6 deg), and two of these three have rounder mass distribution (similar to e.g., Rusu et al. 2016; Shajib et al. 2019). Those with $q < q_{\text{light}}$ have either nearby galaxies or are subject to imperfect lens light subtraction.

6.2. Nature of the sources

The Baldwin-Phillips-Terlevich (BPT) diagram is commonly used to separate the star-forming galaxy population and AGNs (Baldwin et al. 1981). It allows us to further investigate the nature of the lensed sources. We measure the emission-line ratios ($[\text{OIII}]/\text{H}\beta$ versus $[\text{NII}]/\text{H}\alpha$) using the spectra as shown in Fig. 3. The flux of each emission line is fitted by a Gaussian, as shown in Fig. 5. Fortunately, we have three candidates with line detection: HSCJ022622–042522, HSCJ023817–054555, and HSCJ144320–012538, though we can only estimate the upper limit of the $[\text{NII}]/\text{H}\alpha$. The resulting line ratios on the BPT diagram are shown in Fig. 6, and the empirical curve (highlighted in dotted curve) provided from Eq. (1) of Kewley et al. (2013) has a functional form:

$$\log([\text{OIII}]/\text{H}\beta) = \frac{0.61}{\log([\text{NII}]/\text{H}\alpha) - 0.02 - 0.1833z_s} + 1.2 + 0.03z_s. \quad (11)$$

Galaxies below the curve are considered as star-forming galaxies and those above the curve are considered as AGNs. We notice that only HSCJ022622–042522 reaches above the curve, showing that the source is likely an AGN.

For HSCJ141136–010216, we detect the Ly α emission only and no other prominent lines, indicative of an AGN, similar to HSCJ115252+004733. Following the method in More et al. (2017), we measure the FWHM of Ly α emission to be 3.9 \AA (as shown in Fig. 7). This translates to a velocity width of 233 km s^{-1} after accounting for the instrumental broadening. The Lyman- α emitters (LAEs) have average velocity widths of $251 \pm 16 \text{ km s}^{-1}$ (Ouchi et al. 2010). Therefore, the source of HSCJ141136–010216 is most likely an LAE, a compact source with finite size rather than an AGN, which is also consistent with the hint of extension seen in the lensed images.

7. Conclusion and discussion

In this work, we present new lens candidates in the HSC survey, selected mainly by CHITAH. We confirm the lens features based on spectroscopic follow-up and lens modeling. We draw the following conclusions:

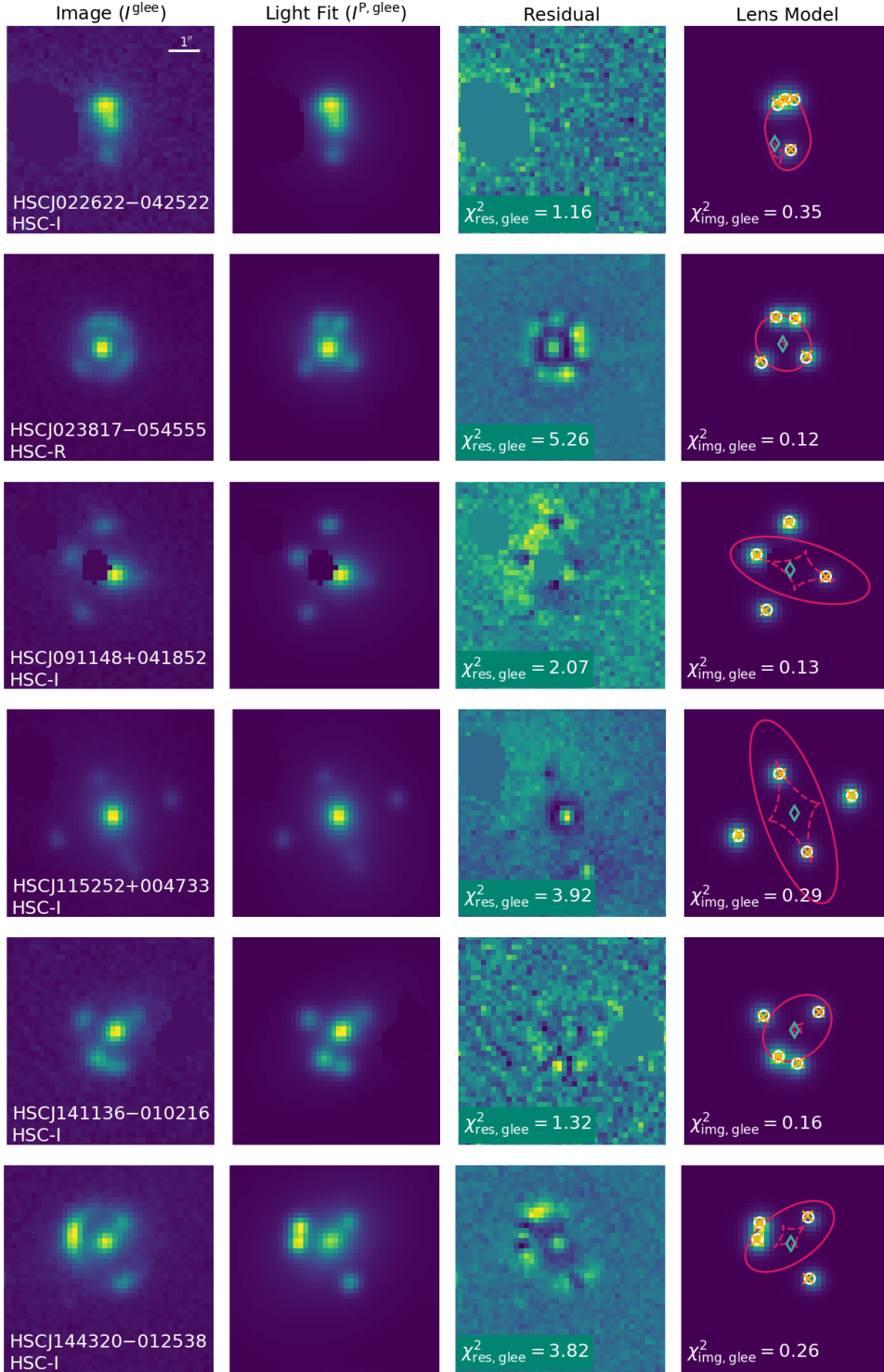


Fig. 4. Best fit of lens modeling from GLEE. *First column:* image in the filter with the sharpest PSF. We further mask out nearby objects. *Second column:* model with a Sérsic light profile and four PSFs, and the residual is shown in the *third column* with the reduced $\chi^2_{\text{res, glee}}$. *Fourth column:* best-fit SIE model. The critical and caustic curves are shown in red solid and dashed lines, respectively. The predicted positions of images and sources are labeled as orange crosses and green diamonds, respectively. The positions of the four PSFs are labeled as white circles. To negate the effects of the nearby galaxy group, we impose external shear for HSCJ022622–042522 to obtain better modeling. Each cutout is $7'' \times 7''$.

- After preselecting objects from either the LRG catalog or the QSO catalog, we employ CHITAH to classify those within the HSC S16A footprint. We obtain 46 lens candidates with grades higher than 1.5, and three of them are previously known lenses which are recovered by CHITAH.
- For spectroscopic observations, we select four high-grade candidates from CHITAH’s classification, which include a known lens presented by More et al. (2017), and two other lenses found by YATTALENS. In total, we obtain X-shooter spectra of six objects and confirm them as lenses.
- The spectroscopic redshifts of lenses and sources are listed in Table 2. We highlight four new redshift measurements for both lens and source.
- We use GLEE to examine the point-like lensed feature of the six confirmed lens systems. HSCJ022622–042522, HSCJ141135–010216, and HSCJ115252+004733 are likely to have point-like sources.
- We plot the BPT diagram to investigate the nature of the lensed source. The position of HSCJ022622–042522 on this diagram suggests that its source is possibly a quasar, though we can only measure the upper limit of the [NII].

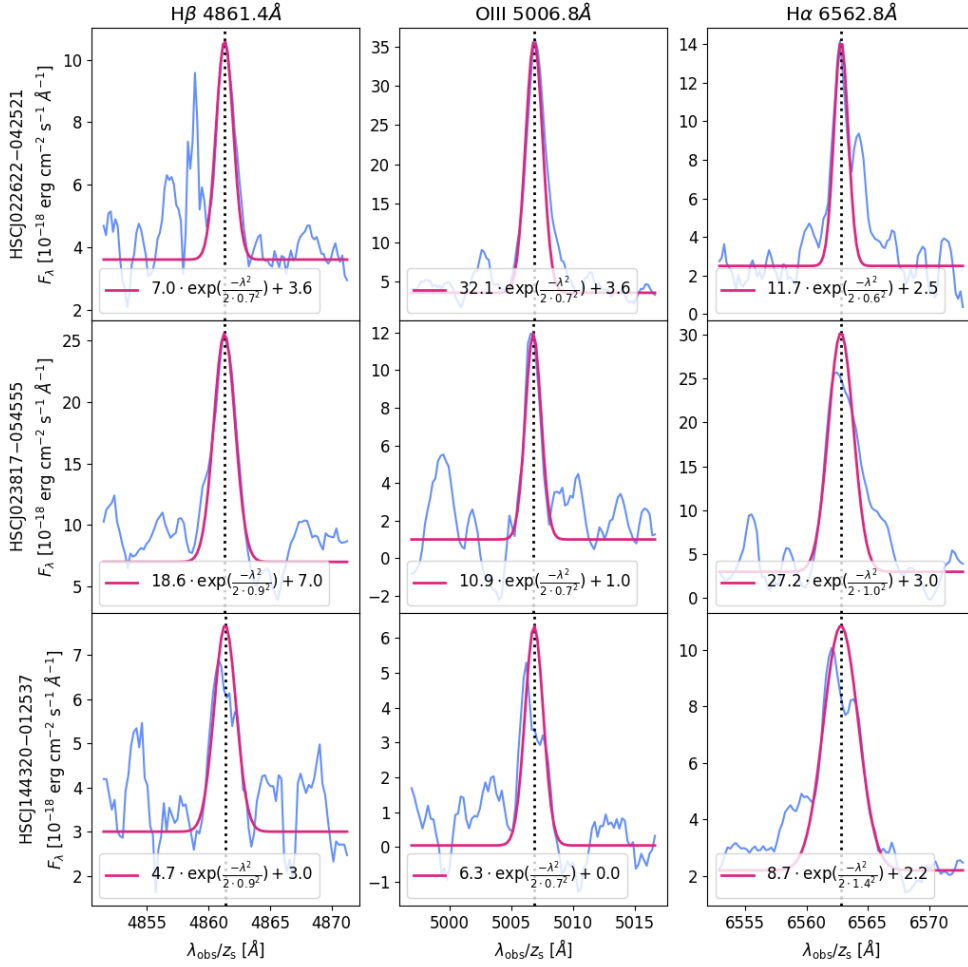


Fig. 5. Fluxes of emission lines: [OIII], H β , and H α . The lines are detected in the X-shooter NIR arm. The red lines show Gaussian fits to the emission lines.

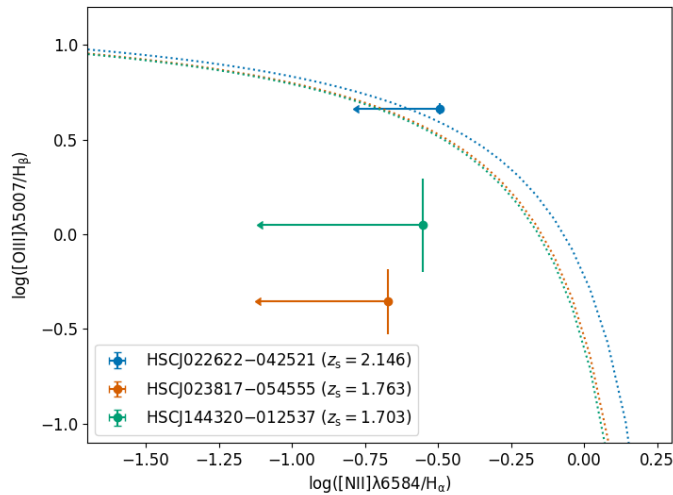


Fig. 6. Baldwin-Phillips-Terlevich diagram showing the division between star-forming galaxies and AGNs. The empirical curve is shown in the dotted curve using Eq. (11): below the curve are star-forming galaxies and above the curve are AGNs.

- We measure the FWHM of Ly α emission for HSCJ 141136–010216 to be $\sim 233 \text{ km s}^{-1}$, showing that it is likely to be a Lyman- α emitter.
- As a result of modeling, we find that the lens mass distribution is rounder but well aligned with the lens light dis-

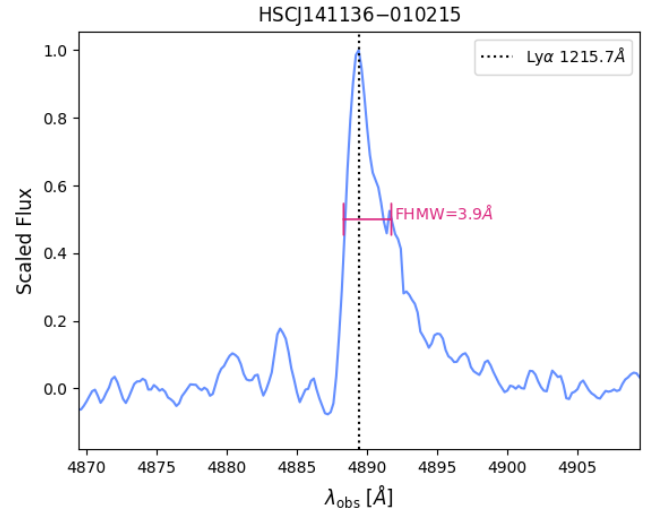


Fig. 7. Ly α emission of HSCJ141136–010216. The red bar shows the FWHM of the emission line.

tribution, except for those sources with nearby galaxies or imperfect light subtraction.

Though only one possible lensed quasar with spectroscopy available is presented in this work, we note that most of our lenses with X-shooter spectra are high-redshift lens systems. These lenses will help us to expand the redshift range for the study of the evolution of lens galaxies.

Acknowledgements. J. H. H. C. acknowledges support from the Swiss National Science Foundation (SNSF). S. H. S. thanks the Max Planck Society for support through the Max Planck Research Group. A. S. acknowledges funding from the European Union's Horizon 2020 research and innovation programme under grant agreement No 792916, as well as a KAKENHI Grant from the Japan Society for the Promotion of Science (JSPS), MEXT, Number JP17K14250. A. T. J. is supported by JSPS KAKENHI Grant Number 17H02868. This work was supported by World Premier International Research Center Initiative (WPI Initiative), MEXT, Japan. A. Y. acknowledges JSPS KAKENHI Grant Number JP25870893. K. C. W. is supported in part by an EACO Fellowship awarded by the East Asia Core Observatories Association, which consists of the Academia Sinica Institute of Astronomy and Astrophysics, the National Astronomical Observatory of Japan, the National Astronomical Observatories of the Chinese Academy of Sciences, and the Korea Astronomy and Space Science Institute. The Hyper Suprime-Cam (HSC) collaboration includes the astronomical communities of Japan and Taiwan, and Princeton University. The HSC instrumentation and software were developed by the National Astronomical Observatory of Japan (NAOJ), the Kavli Institute for the Physics and Mathematics of the Universe (Kavli IPMU), the University of Tokyo, the High Energy Accelerator Research Organization (KEK), the Academia Sinica Institute for Astronomy and Astrophysics in Taiwan (ASIAA), and Princeton University. Funding was contributed by the FIRST program from Japanese Cabinet Office, the Ministry of Education, Culture, Sports, Science and Technology (MEXT), the Japan Society for the Promotion of Science (JSPS), Japan Science and Technology Agency (JST), the Toray Science Foundation, NAOJ, Kavli IPMU, KEK, ASIAA, and Princeton University. The Pan-STARRS1 Surveys (PS1) have been made possible through contributions of the Institute for Astronomy, the University of Hawaii, the Pan-STARRS Project Office, the Max-Planck Society and its participating institutes, the Max Planck Institute for Astronomy, Heidelberg and the Max Planck Institute for Extraterrestrial Physics, Garching, The Johns Hopkins University, Durham University, the University of Edinburgh, Queen's University Belfast, the Harvard-Smithsonian Center for Astrophysics, the Las Cumbres Observatory Global Telescope Network Incorporated, the National Central University of Taiwan, the Space Telescope Science Institute, the National Aeronautics and Space Administration under Grant No. NNX08AR22G issued through the Planetary Science Division of the NASA Science Mission Directorate, the National Science Foundation under Grant No. AST-1238877, the University of Maryland, and Eotvos Lorand University (ELTE). This paper makes use of software developed for the Large Synoptic Survey Telescope. We thank the LSST Project for making their code available as free software at <http://dm.lsst.org>. Based in part on data collected at the Subaru Telescope and retrieved from the HSC data archive system, which is operated by the Subaru Telescope and Astronomy Data Center at National Astronomical Observatory of Japan. This work is based in part on observations collected at the European Southern Observatory under ESO programme 099.A-0220.

References

- Abolfathi, B., Aguado, D. S., Aguilar, G., et al. 2018, *ApJS*, **235**, 42
- Agnello, A. 2017, *MNRAS*, **471**, 2013
- Agnello, A., Treu, T., Ostrovski, F., et al. 2015, *MNRAS*, **454**, 1260
- Aihara, H., Armstrong, R., Bickerton, S., et al. 2018, *PASJ*, **70**, S8
- Anguita, T., Faure, C., Kneib, J. P., et al. 2009, *A&A*, **507**, 35
- Baldwin, J. A., Phillips, M. M., & Terlevich, R. 1981, *PASP*, **93**, 5
- Bonvin, V., Courbin, F., Suyu, S. H., et al. 2017, *MNRAS*, **465**, 4914
- Bosch, J., Armstrong, R., Bickerton, S., et al. 2018, *PASJ*, **70**, S5
- Brescia, M., Cavuoti, S., & Longo, G. 2015, *MNRAS*, **450**, 3893
- Chan, J. H. H., Suyu, S. H., Chiueh, T., et al. 2015, *ApJ*, **807**, 138
- Chao, D. C. Y., Chan, J. H. H., Suyu, S. H., et al. 2019, ArXiv e-prints [arXiv:1910.01140]
- Chen, G. C. F., Fassnacht, C. D., Suyu, S. H., et al. 2019, *MNRAS*, **490**, 1743
- Courbin, F., Chantry, V., Revaz, Y., et al. 2011, *A&A*, **536**, A53
- Dai, X., & Guerras, E. 2018, *ApJ*, **853**, L27
- Dalal, N., & Kochanek, C. S. 2002, *ApJ*, **572**, 25
- Delchambre, L., Krone-Martins, A., Wertz, O., et al. 2019, *A&A*, **622**, A165
- Dobos, L., Csabai, I., Yip, C.-W., et al. 2012, *MNRAS*, **420**, 1217
- Ducourant, C., Delchambre, L., Finet, F., et al. 2018a, in *Astrometry and Astrophysics in the Gaia Sky*, eds. A. Recio-Blanco, P. de Laverny, A. G. A. Brown, & T. Prusti, *IAU Symp.*, **330**, 59
- Ducourant, C., Wertz, O., Krone-Martins, A., et al. 2018b, *A&A*, **618**, A56
- Freedman, W. L., Madore, B. F., Hatt, D., et al. 2019, *ApJ*, **882**, 34
- Freudling, W., Romaniello, M., Bramich, D. M., et al. 2013, *A&A*, **559**, A96
- Furusawa, H., Koike, M., Takata, T., et al. 2018, *PASJ*, **70**, S3
- Gilman, D., Birrer, S., Treu, T., Nierenberg, A., & Benson, A. 2019, *MNRAS*, **487**, 5721
- Inada, N., Becker, R. H., Burles, S., et al. 2003, *AJ*, **126**, 666
- Inada, N., Oguri, M., Becker, R. H., et al. 2008, *AJ*, **135**, 496
- Inada, N., Oguri, M., Shin, M.-S., et al. 2010, *AJ*, **140**, 403
- Inada, N., Oguri, M., Shin, M.-S., et al. 2012, *AJ*, **143**, 119
- Jackson, N., Rampadarath, H., Ofek, E. O., Oguri, M., & Shin, M.-S. 2012, *MNRAS*, **419**, 2014
- Kawanomoto, S., Uruguchi, F., Komiyama, Y., et al. 2018, *PASJ*, **70**, 66
- Kazin, E. A., Blanton, M. R., Scoccamarro, R., et al. 2010, *ApJ*, **710**, 1444
- Kewley, L. J., Maier, C., Yabe, K., et al. 2013, *ApJ*, **774**, L10
- Kochanek, C. S., Mochejska, B., Morgan, N. D., & Stanek, K. Z. 2006, *ApJ*, **637**, L73
- Komiyama, Y., Obuchi, Y., Nakaya, H., et al. 2018, *PASJ*, **70**, S2
- Krone-Martins, A., Delchambre, L., Wertz, O., et al. 2018, *A&A*, **616**, L11
- Lemon, C. A., Auger, M. W., McMahon, R. G., & Kposov, S. E. 2017, *MNRAS*, **472**, 5023
- Lemon, C. A., Auger, M. W., McMahon, R. G., & Ostrovski, F. 2018, *MNRAS*, **479**, 5060
- Lemon, C. A., Auger, M. W., & McMahon, R. G. 2019, *MNRAS*, **483**, 4242
- Marshall, P. J., Hogg, D. W., Moustakas, L. A., et al. 2009, *ApJ*, **694**, 924
- Marshall, P. J., Verma, A., More, A., et al. 2016, *MNRAS*, **455**, 1171
- Mineshige, S., & Yonehara, A. 1999, *PASJ*, **51**, 497
- Miyazaki, S., Oguri, M., Hamana, T., et al. 2018, *PASJ*, **70**, S27
- More, A., Verma, A., Marshall, P. J., et al. 2016, *MNRAS*, **455**, 1191
- More, A., Lee, C.-H., Oguri, M., et al. 2017, *MNRAS*, **465**, 2411
- Myers, S. T., Jackson, N. J., Browne, I. W. A., et al. 2003, *MNRAS*, **341**, 1
- Nierenberg, A. M., Treu, T., Brammer, G., et al. 2017, *MNRAS*, **471**, 2224
- Oguri, M. 2010, *PASJ*, **62**, 1017
- Oguri, M., Inada, N., Pindor, B., et al. 2006, *AJ*, **132**, 999
- Oguri, M., Inada, N., Strauss, M. A., et al. 2008, *AJ*, **135**, 512
- Oguri, M., Inada, N., Strauss, M. A., et al. 2012, *AJ*, **143**, 120
- Ostrovski, F., McMahon, R. G., Connolly, A. J., et al. 2017, *MNRAS*, **465**, 4325
- Ouchi, M., Shimasaku, K., Furusawa, H., et al. 2010, *ApJ*, **723**, 869
- Planck Collaboration VI. 2020, *A&A*, in press, <https://doi.org/10.1051/0004-6361/201833910>
- Poindexter, S., Morgan, N., & Kochanek, C. S. 2008, *ApJ*, **673**, 34
- Røfsdal, S. 1964, *MNRAS*, **128**, 307
- Reid, B., Ho, S., Padmanabhan, N., et al. 2016, *MNRAS*, **455**, 1553
- Richards, G. T., Nichol, R. C., Gray, A. G., et al. 2004, *ApJS*, **155**, 257
- Riess, A. G., Casertano, S., Yuan, W., Macri, L. M., & Scolnic, D. 2019, *ApJ*, **876**, 85
- Rusu, C. E., Oguri, M., Minowa, Y., et al. 2016, *MNRAS*, **458**, 2
- Shajib, A. J., Birrer, S., Treu, T., et al. 2019, *MNRAS*, **483**, 5649
- Silverman, B. W. 1986, *Density Estimation for Statistics and Data Analysis* (London: Chapman and Hall)
- Sonnenfeld, A., Chan, J. H. H., Shu, Y., et al. 2018, *PASJ*, **70**, S29
- Sonnenfeld, A., Jaelani, A. T., Chan, J. H. H., et al. 2019, *A&A*, **630**, A71
- Suyu, S. H., & Halkola, A. 2010, *A&A*, **524**, A94
- Suyu, S. H., Marshall, P. J., Auger, M. W., et al. 2010, *ApJ*, **711**, 201
- Suyu, S. H., Hensel, S. W., McKean, J. P., et al. 2012, *ApJ*, **750**, 10
- Suyu, S. H., Auger, M. W., Hilbert, S., et al. 2013, *ApJ*, **766**, 70
- van Dokkum, P. G. 2001, *PASP*, **113**, 1420
- Vegetti, S., Lagattuta, D. J., McKean, J. P., et al. 2012, *Nature*, **481**, 341
- Vernet, J., Dekker, H., D'Odorico, S., et al. 2011, *A&A*, **536**, A105
- Williams, P. R., Agnello, A., Treu, T., et al. 2018, *MNRAS*, **477**, L70
- Wong, K. C., Sonnenfeld, A., Chan, J. H. H., et al. 2018, *ApJ*, **867**, 107
- Wong, K. C., Suyu, S. H., Chen, G. C. F., et al. 2019, *MNRAS*, submitted [arXiv:1907.04869]
- Wyithe, J. S. B., Webster, R. L., & Turner, E. L. 2000, *MNRAS*, **315**, 51
- Yonehara, A., Mineshige, S., Manmoto, T., et al. 1998, *ApJ*, **501**, L41